applied mechanics

Article

Numerical Investigation of Hardfacing Process Parameters for Gate Valve Restoration with Experimental Characterization of Hardfaced Specimens

Riza Gabdyssalyk [1,*], Daulet Zhamsap [1], Samat Baigereyev [1,*], Karibek Sherov [2], Alfiya Muzdybayeva [1] and Tatyana Brim [1]

[1] International School of Engineering, D. Serikbayev East Kazakhstan Technical University, Ust-Kamenogorsk 070003, Kazakhstan; legendaulet@gmail.com (D.Z.); amuzdybaeva@edu.ektu.kz (A.M.); tbrim@edu.ektu.kz (T.B.)
[2] Department of «Technological Machines and Equipment», S. Seifullin Kazakh Agro Technical Research University, Astana 010011, Kazakhstan; k.sherov@kazatu.edu.kz
* Correspondence: rgabdysalyk@edu.ektu.kz (R.G.); sbaigereyev@edu.ektu.kz (S.B.); Tel.: +7-777-148-62-78 (R.G.); +7-777-411-96-50 (S.B.)

Abstract

Hardfacing is widely used to restore worn gate-valve surfaces, but the choice of process parameters must account for residual stress, distortion, plastic strain, and the heat-affected zone (HAZ). This study investigated the hardfacing of 09G2S steel numerically in Simufact Welding using a Taguchi L9 design for three filler materials, Np-65G, Stoodite 6M, and PrNl-3V14K, giving 27 simulated conditions. The Goldak heat source was calibrated against a theoretical penetration depth of 1.2–1.5 mm. Conditions resulting in metal boiling, an unmelted bead center, or a penetration depth outside 1.0–2.0 mm were excluded. Lower residual stresses were obtained only together with insufficient penetration or overheating. Run 6 was selected for Np-65G (285 MPa; HAZ depth, 4.7 mm) and Stoodite 6M (373 MPa; 4.6 mm), and Run 2 for PrNl-3V14K (289 MPa; 3.5 mm). On a model of a 90-mm-thick gate plate, the selected Np-65G condition gave a penetration depth of only about 0.5 mm; an adjusted condition within the investigated levels (160 A, 12 V, 3 m/h, 200 °C) gave 1.45–1.80 mm with a fully melted bead for both Np-65G and Stoodite 6M. Conditions selected on specimens must therefore be reassessed for the actual component. Specimens hardfaced under industrial conditions were characterized by microscopy and microhardness testing: 386–466 HV0.05 for the Stoodite 6M deposit and 345–440 HV0.05 for Np-65G.

Keywords: hardfacing; gate valve restoration; thermomechanical simulation; Simufact Welding; Taguchi L9 design; heat-affected zone; residual stress; microhardness

Received: 12 October 2026
Revised: 2 November 2026
Accepted: 11 November 2026
Published: 15 November 2026

Copyright: © 2026 by the authors. Licensee MDPI, Basel, Switzerland. This article is an open access article distributed under the terms and conditions of the Creative Commons Attribution (CC BY) license.

1. Introduction

Gate valves are widely used in pipeline systems, where the condition of the sealing surfaces directly affects reliable operation. During service, gate and sealing components are exposed to contact loading, friction, abrasive particles, corrosion, and gradual wear. As the working surfaces deteriorate, sealing performance may decrease and the component may eventually require replacement. For large valve components, replacement can

involve considerable cost and equipment downtime. Restoration of worn working surfaces is therefore of practical interest, particularly for valves operating under demanding conditions.

Hardfacing is commonly used to restore worn surfaces and, at the same time, modify their surface properties. The quality of the deposited layer depends on both the filler material and the conditions under which the layer is formed. Welding current, arc voltage, travel speed, preheating temperature, and the resulting heat input affect penetration, dilution, temperature distribution, cooling conditions, residual stresses, deformation, and microstructural development. These effects make the selection of hardfacing parameters an important part of the restoration procedure.

A number of studies have examined hardfacing and related surface-deposition methods for valve components. Klimpel et al. [1] studied laser and plasma surfacing of engine-valve faces using cobalt-based powders. Their results showed that the heat source and processing parameters influence the geometry of the deposited layer and its interaction with the substrate. Dilution was identified as an important factor because excessive incorporation of the base metal into the deposited layer alters the composition and properties of the deposited metal. Yu et al. [2] compared different hardfacing processes using cobalt-based alloys and demonstrated differences in microstructure and corrosion behavior. Fu et al. [3] investigated an iron-based coating for the sealing surface of a nuclear power plant valve and achieved improved wear and corrosion resistance. Ding et al. [4] applied laser hardfacing with a mixture of Stellite alloys directly to the sealing surfaces of control valve seats, while Que et al. [5] investigated cracking and the microstructure of cobalt-free hardfacing on valve seats.

Research specifically related to wedge gate valves has also shown the potential of hardfacing. Mussina et al. [6] investigated components hardfaced with Sv-10Kh17T welding wire under dry friction and in water- and oil-based media. The hardfaced samples showed higher wear resistance and microhardness and lower friction compared with the untreated material. Such experimental studies provide useful information about the final surface condition, including hardness, wear, corrosion behavior, microstructure, and tribological characteristics. However, they provide less information about the thermal and stress–strain processes that occur while the deposited layer is being formed. In the authors' previous study [7], the effects of TIG hardfacing parameters on the microstructure and dilution ratio of the deposited layer on low-alloy steel shut-off valve seats were investigated experimentally. The present study differs in that the process parameters are selected numerically according to physical feasibility criteria and subsequently applied to a model of the gate plate.

Numerical modeling can provide additional information about these processes. Sachajdak et al. [8] developed a thermal model of gas metal arc hardfacing and used it to predict temperature distributions and thermal cycles. The model was compared with thermographic measurements, illustrating the importance of experimental verification when numerical results are used to describe the thermal history of a hardfacing process. This is relevant to gate-valve restoration because thermal conditions in an actual valve component may differ from those obtained using a simple flat specimen.

Numerical welding studies have also moved beyond thermal analysis alone. Guo et al. [9] used Simufact Welding to model a layered bimetallic TIG–MIG welding process and analyzed temperature, residual stresses, and deformation. Wei et al. [10] applied the same software together with a moving double-ellipsoidal heat source for simulation of thick-plate welding. Their study linked the calculated temperature field with the resulting residual stress distribution. Although these works did not investigate gate-valve hardfacing, they demonstrate that Simufact Welding can be used to analyze the coupled thermal and mechanical response produced by a moving welding heat source.

https://doi.org/10.3390/applmech7040098

The definition and calibration of the heat source remain important for this type of modeling. Da Silva et al. [11] combined numerical modeling with welding experiments and physical simulation in a study of the heat-affected zone in superduplex stainless steel. The calculated thermal cycles and fusion-zone geometry were compared with experimental data before further numerical analysis was performed. Li et al. [12] used a three-dimensional multiphysics model for submerged-arc surfacing and considered temperature, stress, phase transformation, and material flow. Their results showed that peak temperature alone is not sufficient to describe the response of a surfaced component, since cooling conditions, thermal gradients, phase transformation, and stress development are interconnected.

Other studies have used similar numerical-experimental approaches for surface engineering processes. Bararpour et al. [13] combined finite-element modeling with experimental investigation of friction surfacing and used the calculated thermomechanical response to interpret the properties of the deposited material. Aminzadeh et al. [14] investigated the relationship between process parameters and residual stress distribution using numerical and statistical methods during the deep drawing of laser-welded blanks—that is, in a metal-forming process rather than a welding process. These studies were conducted for different materials and processes, but they illustrate how numerical simulation can be used to reduce the experimental search space and to examine relationships that are difficult to obtain from physical trials alone. Numerical simulation has also been applied directly to hardfacing: to restore a worn grinding roller [15], to determine hardfacing process parameters [16], and to calculate temperature, stress, and deformation distributions during the hardfacing of splined shafts [17].

Despite the amount of work devoted to hardfacing and welding simulation, the two directions are still not fully integrated for the restoration of gate-valve working surfaces. Experimental studies of valve components have focused mainly on the properties of hardfaced layers [1–7], whereas numerical studies have predominantly examined other welded and hardfaced structures [8–13,15–17] or other metal-forming processes [14]. In particular, there is still limited information on how hardfacing parameters affect the thermomechanical response of a 09G2S steel gate component and how numerically selected conditions can be transferred to an industrial hardfacing process.

This issue is relevant because several responses have to be considered at the same time. A suitable hardfacing condition should provide adequate deposition and bonding, but excessive heat input may enlarge the heat-affected zone, increase deformation and residual stresses, and affect the structure of the substrate. A parameter combination that is favorable with respect to one response may therefore be less favorable with respect to another.

In the present study, hardfacing process parameters for gate-valve restoration were investigated numerically, and specimens hardfaced under industrial conditions were characterized experimentally. Simulations were performed in Simufact Welding for 09G2S steel using three hardfacing materials: Np-65G, Stoodite 6M, and PrNl-3V14K. The designations Np-65G and PrNl-3V14K are Latin transliterations of the corresponding GOST material grades and are used throughout this paper for consistency. Welding current, arc voltage, travel speed, and preheating temperature were varied according to a Taguchi L9 design. Equivalent stresses, displacements, plastic strain, temperature response, penetration depth, and heat-affected zone (HAZ) depth were compared for the investigated parameter combinations.

The present study differs from previous welding and hardfacing simulation studies [8–13,15–17] in three respects. First, the heat source was calibrated to a specified penetration depth in the base metal, and the same calibrated heat source was used in all 27 simu-

lations. Second, before ranking, the simulations were screened for physical feasibility: conditions resulting in metal boiling, an unmelted central region of the deposited bead, or a penetration depth outside the process window were excluded. Third, the relative sensitivity of the responses to each process parameter was assessed descriptively from the factor sums of squares, and the selected condition was applied to a gate-plate model to assess its transferability to the actual component.

The numerical stage was used to identify comparatively favorable process conditions rather than to determine a global mathematical optimum. Specimens hardfaced under industrial conditions were examined by optical and scanning electron microscopy and microhardness testing; these measurements characterize the hardfaced layers but do not constitute a quantitative validation of the model.

2. Materials and Methods

2.1. Research Framework and Materials

The study combined numerical simulation with the examination of specimens hardfaced under industrial conditions. The numerical part was used to investigate the effects of the main process parameters on the thermomechanical response of the substrate and to identify favorable parameter combinations. The hardfaced specimens were examined to characterize the resulting layers. The overall workflow of the study is shown in Figure 1.

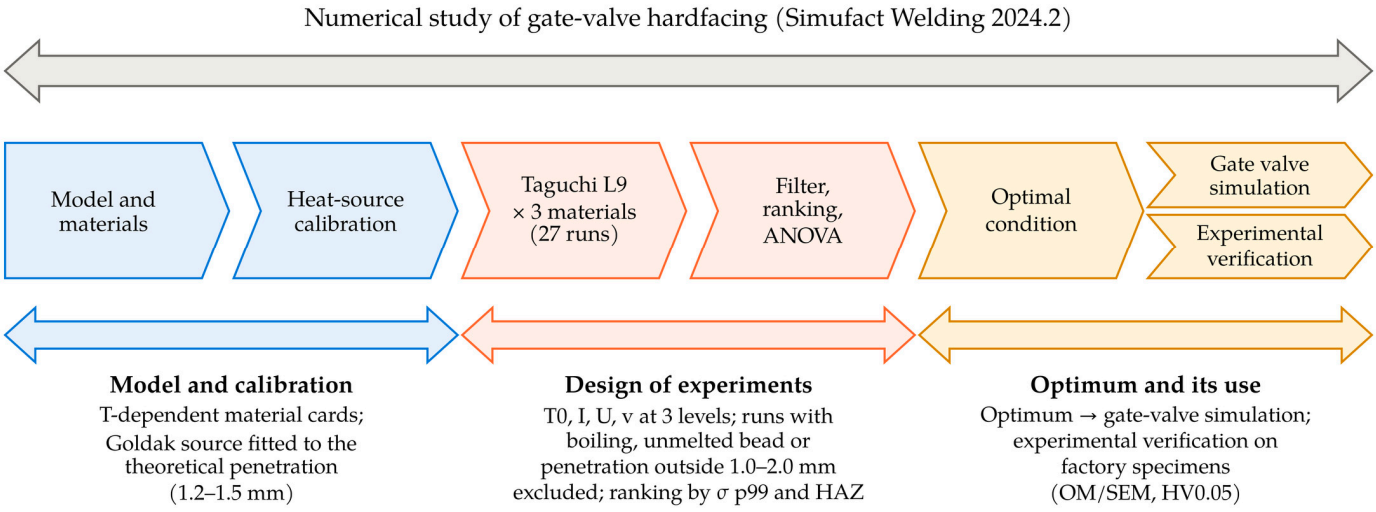


Figure 1. Study workflow: model development and heat-source calibration; Taguchi L9 design for three hardfacing materials; screening of physically feasible process conditions; ranking and ANOVA-based descriptive factor-sensitivity analysis for the saturated L9 design; selection of comparatively favorable conditions; assessment and adjustment of the selected conditions using the gate-plate model; and experimental characterization of industrially hardfaced specimens.

The gate-valve components considered in this study are intended for oil and gas applications. During operation, the gate is subjected to repeated mechanical loading, friction against the valve seats, and abrasive action of particles carried by the working medium. These conditions gradually damage the working surface. Hardfacing can therefore be considered as a restoration method that may reduce the need for complete replacement of worn components.

The substrate material was low-alloy structural steel 09G2S. Specimens measuring 20 × 20 × 70 mm were used both in the numerical simulations and in the experimental hardfacing trials. Using the same specimen dimensions in both stages made it possible to maintain comparable geometrical conditions.

Three hardfacing materials were considered: Np-65G hardfacing wire, the cobalt-based alloy Stoodite 6M, and the hardfacing alloy PrNl-3V14K. All three hardfacing materials were manufactured by Beijing Hugetall Sciences & Technology Co., Ltd. (Beijing, China) and supplied by Individual Entrepreneur NB Market (Almaty, Kazakhstan). Np-65G and PrNl-3V14K were specified in accordance with GOST 10543-98 and GOST 21449-75, respectively, whereas Stoodite 6M was specified in accordance with AWS A5.21. These materials differ in composition and intended application and were selected to compare their influence on the thermomechanical response of the 09G2S substrate. In the numerical model, temperature-dependent thermophysical and mechanical properties were assigned to both the substrate and deposited materials. The properties included density, specific heat capacity, thermal conductivity, and the mechanical characteristics available in the simulation database. The sources of the material property data are provided in Section 2.2.

2.2. Numerical Model of the Hardfacing Process

Numerical simulations were performed in Simufact Welding 2024.2.0 (Hexagon Manufacturing Intelligence GmbH, Hamburg, Germany) using the MSC Marc solver. A three-dimensional rectangular specimen corresponding to the geometry of the experimental specimens was used as the computational domain. A deposited bead was modeled on the upper surface of the substrate to reproduce the localized thermal effect of the hardfacing process (width: 10 mm; height: 1.36 mm; length: 49 mm; Figure 2).

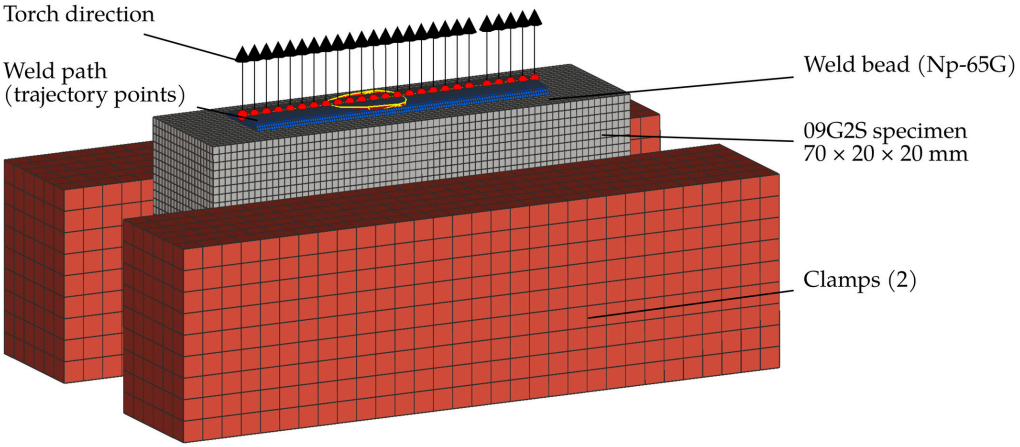


Figure 2. Numerical model of the specimen used for hardfacing simulation in Simufact Welding: 09G2S steel substrate (gray), deposited bead (blue), and two clamps (red); the red dots indicate the welding path, the black arrows indicate the torch travel direction, and the yellow ellipse represents the Goldak heat source.

The welding arc was modeled using the Goldak double-ellipsoidal heat source [18]. This model describes the heat distribution in the front and rear parts of the moving source and is widely used in welding simulations. Numerical models have also been used in hardfacing studies to examine temperature and residual stress development during heating and cooling [19,20]. Previous studies have also shown that the selected heat-source parameters can affect the calculated temperature field and HAZ dimensions [21,22].

The heat-flux density q_i in the front ($i = f$) and rear ($i = r$) regions of the heat source was defined by the following expression:

$$q_i(x,y,z) = \frac{2f_i Q k^{3/2}}{a_i b d \pi^{3/2}} \exp\left(-\frac{kx^2}{a_i^2} - \frac{ky^2}{b^2} - \frac{kz^2}{d^2}\right), \qquad Q = \eta UI,$$

where a_f, a_r—are the front and rear semi-axis lengths, respectively, b—is the half-width, d—is the depth, $f_f + f_r = 2$, k—is the distribution concentration parameter (k = 3 in the original formulation [18]), η—is the arc efficiency. The product P = UI is referred to below as the arc power. In this study, k = 2 was adopted: during calibration, k = 2 and k = 3 were tested together with the source dimensions, and the adopted parameter set satisfied all three calibration conditions described below.

Four process parameters were varied in the simulations:

- welding current, I;
- arc voltage, U;
- travel speed, v;
- substrate preheating temperature, T.

These parameters influence the amount of heat introduced into the substrate and, as a result, affect the temperature field, heat-affected zone, residual stresses, and deformation.

The parameter ranges were defined separately for each hardfacing material based on the technological ranges considered in this study. The current, voltage, and preheating-temperature levels cover the process window for hardfacing with the respective material, whereas the travel-speed levels were defined theoretically as ±25% of the speed at which the calibrated heat source produced the target penetration depth (4 m/h for Np-65G and Stoodite 6M, and 10 m/h for PrNl-3V14K). The resulting process-parameter levels are listed in Table 1.

Table 1. Process parameter levels used in the numerical investigation.

Hardfacing Material	Level	Current, A	Voltage, V	Travel Speed, m/h	Preheating Temperature, °C
PrNl-3V14K	L1	160	11	8	200
PrNl-3V14K	L2	180	12.5	10	225
PrNl-3V14K	L3	200	14	12	250
Stoodite 6M	L1	120	10	3	150
Stoodite 6M	L2	140	12	4	175
Stoodite 6M	L3	160	14	5	200
Np-65G	L1	120	10	3	180
Np-65G	L2	140	12	4	190
Np-65G	L3	160	14	5	200

The thermal and mechanical analyses were coupled so that the temperature history and the resulting stress–strain response of the specimen could be evaluated during heating and cooling. Temperature-dependent material properties were included to represent changes in material behavior over the thermal cycle. Similar numerical-experimental welding studies have used thermal-structural analysis to examine temperature, deformation, and residual stresses and to compare the calculated response with experimental measurements [23,24].

Material properties were specified using standards and technical data sheets. For 09G2S steel, the elastic modulus and yield strength were taken from GOST 34233.1-2017 [25]; the thermophysical properties and coefficient of thermal expansion at elevated temperatures were taken from EN 1993-1-2 [26]; and the solidus and liquidus temperatures were obtained from the model presented in [27]. For Np-65G, the properties of the corresponding steel grade 65G were used: the elastic modulus, thermal expansion, thermal conductivity, specific heat, and density were taken from reference data for this grade; the room-temperature yield strength (690 MPa) corresponds to the quenched-and-tempered

condition and was chosen to match the hardness specified for Np-65G deposits; the solidus and liquidus temperatures (1370 and 1474 °C) were obtained from [27]; and the decrease in yield strength with temperature followed the Simufact library data for S355 steel. The adopted Np-65G material card combined reference data for grade 65G, the solidus and liquidus temperatures obtained from [27], and the temperature dependence of yield strength from the Simufact S355 library. Because these inputs do not constitute a single experimentally verified temperature-dependent dataset for Np-65G, the resulting thermomechanical predictions should be interpreted comparatively rather than as exact material-specific values. Because temperature-dependent data for the actual Stoodite 6M and PrNl-3V14K hardfacing materials were unavailable, the properties of analogous alloys—Stellite 6 [28] and Stellite 1 [29], respectively—were used in the simulations. This represents a modeling assumption rather than measured properties of the hardfacing materials. The coefficient of thermal expansion was specified as a true (instantaneous) value and set to zero above the solidus temperature. All model settings are listed in Table 2.

Table 2. Numerical model settings.

Parameter	Value
Software and solver	Simufact Welding 2024.2.0 (MSC Marc solver); non-stationary thermomechanical problem; parallel calculation on 6 cores
Specimen	09G2S steel bar 70 × 20 × 20 mm; one deposited bead 10 × 1.36 mm long 49 mm (x = 10–59 mm)
Mesh	Eight-node hexahedra with an edge of 1 mm: 27,314 elements, 33,096 nodes (base 22,400 elements, deposited bead 4914 elements)
Base metal	09G2S: temperature-dependent thermophysical and elasto-plastic properties [25–27]; solidus 1460 °C
Surfacing materials	Np-65G (solidus 1370 °C); Stoodite 6M—properties of Stellite 6 alloy (solidus 1285 °C) [28]; PrNl-3V14K—analog of Stellite 1 (solidus 1248 °C) [29]
Phase transformations	Not modeled
Heat source	Goldak double ellipsoid: η = 0.77 [30]; b = 4.5 mm; d = 3.5 mm; af = 2.7 mm; ar = 9.9 mm; k = 2
Source calibration	The target (theoretical) penetration is 1.2–1.5 mm; at least 95% of the nodes in the central 60% of the bead width are melted; Tmax is below the boiling point of iron (2861 °C). Result: penetration depth 1.42/1.36/1.41 mm, Tmax 2450/2377/2673 °C (Np-65G/Stoodite 6M/PrNl-3V14K)
Thermal boundary conditions	Convection h = 20 W/(m²·K), ambient temperature 20 °C; radiation, emissivity 0.6; heat exchange with clamps 1000 W/(m²·K)
Mechanical boundary conditions	Two clamps from 0 to 900 s; after their removal, a statically determinate 3-2-1 constraint scheme at the three corners of the lower face
Time step	Deposition time set by the travel speed of each run; cooling with a maximum time step of 120 s; end of the calculation at 1200 s (maximum specimen temperature 22–32 °C)
Responses	99th percentile of von Mises equivalent stress in the middle part of the deposited bead (x = 20–50 mm); HAZ depth beyond the fusion boundary (peak temperature isotherms of 1460 and 725 °C); melting; residual distortion after removal of rigid-body motion and uniform shrinkage; equivalent plastic strain (99th percentile in the middle part of the deposited bead)

The heat-source parameters cannot be measured directly and were therefore calibrated. The initial calibration target was a theoretical base-metal penetration depth of 1.2–1.5 mm, which ensures fusion without excessive dilution of the hardfaced layer. The arc efficiency was set to 0.77, corresponding to the average value reported for gas tungsten

arc welding (GTAW/TIG welding) in the review [30]. The heat-source half-width was selected to be close to the weld-pool half-width, as recommended by Goldak and Akhlaghi [31]. The heat source was considered calibrated when all three conditions listed in Table 2 were satisfied simultaneously. One set of heat-source parameters satisfied these conditions for all three materials and remained unchanged throughout the entire L9 series; only the process parameters were varied.

The mechanical boundary conditions were selected so as not to introduce additional stresses into the specimen. During hardfacing and subsequent cooling up to 900 s, the specimen was held by two clamps. After the clamps were removed, a statically determinate 3-2-1 constraint scheme was applied [32]: three, two, and one translational degrees of freedom were constrained at three respective corners of the bottom surface. This constraint scheme eliminates the six rigid-body degrees of freedom without restricting free shrinkage or bending; therefore, the support reactions do not contribute to the residual stresses.

2.3. Design of the Numerical Investigation

A Taguchi L9 orthogonal array [33,34] was used to examine four process parameters at three levels. This design reduced the number of required simulations while still allowing the different parameter combinations to be compared. Nine simulations were carried out for each hardfacing material, giving a total of 27 simulations for the three materials.

The L9 design is presented in Table 3. The numerical values assigned to levels L1-L3 for each material are given in Table 1.

Table 3. Taguchi L9 arrangement used for the numerical investigation.

Run	Preheating Temperature	Current	Voltage	Travel speed
1	L1	L1	L1	L1
2	L1	L2	L2	L2
3	L1	L3	L3	L3
4	L2	L1	L2	L3
5	L2	L2	L3	L1
6	L2	L3	L1	L2
7	L3	L1	L3	L2
8	L3	L2	L1	L3
9	L3	L3	L2	L1

This design allowed the three hardfacing materials to be studied using comparable combinations of low, intermediate, and high parameter levels without performing a full-factorial set of simulations.

In this study, the Taguchi design was used mainly for parameter screening and comparison, rather than for determination of a global mathematical optimum. The parameter combinations were compared using their calculated thermomechanical responses, and the most favorable conditions within the investigated ranges were selected for further assessment.

2.4. Simulation Output and Data Processing

After each simulation, the results were exported from Simufact Welding for further analysis. The calculations were automated through the embedded Python API in Simufact Welding 2024.2.0, based on Python 3.10.8. The simulation results were processed and visualized using custom Python scripts with NumPy, pandas, Matplotlib, and PyVista. A simulation was included in the analysis only if the solver terminated normally and the time of the final step coincided with the specified end time of the simulation (1200 s).

The following response variables were evaluated:

- Peak temperature throughout the entire model, including the substrate and deposited bead;
- penetration depth—the maximum depth below the original substrate surface reached by the 1460 °C peak-temperature isotherm, corresponding to the solidus temperature of 09G2S steel; the depth was obtained by linear interpolation of the nodal peak temperature along each vertical line of nodes;
- fraction of the bead center melted—the fraction of nodes within the central 60% of the bead width at which the peak temperature exceeded the solidus temperature of the filler material. This fraction was computed during post-processing rather than in Simufact: the nodal peak temperatures exported in UNV format were read with a Python script, and the bead nodes within the central 60% of the bead width in the region x = 20–50 mm were counted;
- HAZ depth beyond the fusion line—the vertical distance between the 1460 °C and 725 °C isotherms, the latter corresponding to the Ac1 temperature of 09G2S steel. Critical temperatures of low-alloy steels can also be estimated from the chemical composition using empirical equations [35]. The HAZ depth was determined along each vertical line in the transverse cross-section, and the maximum value is reported in the tables;
- residual von Mises equivalent stress—the 99th percentile of the nodal values in the central region of the bead (x = 20–50 mm) at the end of the simulation;
- distortion—the maximum residual displacement after removing the rigid-body motion of the specimen [36,37] and its uniform shrinkage [38];
- equivalent plastic strain—the 99th percentile of the values in the central region of the bead (x = 20–50 mm). The maximum value at an individual node was not used because it is sensitive to local mesh characteristics.

These variables describe different aspects of the thermal and mechanical response of the specimen during hardfacing. Equivalent stress and equivalent plastic strain were used to evaluate the mechanical response, whereas distortion was used to characterize changes in the specimen geometry during heating and cooling. The central region of the bead was selected to exclude arc ignition and extinction effects at its ends. The 99th percentile was used instead of the maximum because the maximum value at an individual node is sensitive to the mesh. The stress tensor and temperature data were matched to the nodes using their node numbers, and the tensor components were read in the order specified by the UNV format.

The HAZ was determined from the calculated peak-temperature field. It was defined as the region of the substrate between the fusion boundary (1460 °C) and the 725 °C isotherm, corresponding to the critical Ac1 temperature of 09G2S steel. Its depth was measured from the fusion line along each vertical line in the transverse cross-section.

The process conditions were compared in terms of penetration depth, residual stress, distortion, equivalent plastic strain, peak temperature, and HAZ depth. Physically infeasible conditions were excluded first. These included conditions with a peak temperature above the boiling point of iron (2861 °C), an unmelted central region of the bead (fewer than 95% of the nodes above the solidus temperature of the filler material), or a penetration depth outside the 1.0–2.0 mm process window. A penetration depth of less than 1 mm creates a risk of lack of fusion, whereas a depth greater than 2 mm results in excessive dilution of the hardfaced layer by the base metal.

The feasible conditions were then ranked using the sum of two normalized responses—residual stress (99th percentile) and HAZ depth—with equal weighting. For each material, each response was normalized to a range of 0–1 over the feasible conditions,

and the condition with the lowest sum was selected. Because these responses did not always vary in the same direction, the condition selected for each material represented a balance among several numerical indicators rather than the minimum of a single parameter.

The relative sensitivity of each response to the investigated factors was estimated descriptively from the factor sums of squares calculated using the complete set of nine simulations for each material. The L9 design with four three-level factors is saturated, the simulations are deterministic and have no replicates, and factor interactions cannot be separated from the main effects. Therefore, the calculated percentage contributions are used only as screening indicators of relative sensitivity within the investigated factor ranges. They are not interpreted as estimates of statistical significance, and no significance tests or confidence intervals are reported.

2.5. Experimental Assessment of the Selected Hardfacing Conditions

Experimental hardfacing trials were carried out at Ust-Kamenogorsk Valve Plant JSC. The experiments used 09G2S steel specimens measuring 20 × 20 × 70 mm, the same dimensions as those used in the numerical model.

The hardfacing conditions were selected by an experienced welding specialist based on arc stability, weld-pool behavior, and the quality of the deposited bead. The welding current, arc voltage, and preheating temperature were within the ranges considered in the numerical study, whereas the travel speeds were higher than the simulated levels; consequently, the heat input in the industrial trials was lower than in the selected simulated conditions. The experiments therefore did not reproduce the simulated conditions and were used to characterize the hardfaced layers rather than to validate the model. The travel speeds of manual TIG hardfacing were not measured; the values given below are estimates.

For Np-65G, hardfacing was performed at a current of approximately 140 A, an arc voltage of 10–14 V, a travel speed of 20–25 m/h, and a preheating temperature of 180 °C. The hardfaced layer was approximately 1.5–2 mm thick. For Stoodite 6M, the corresponding process conditions were approximately 140 A, 11 V, 8–12 m/h, and 150 °C, with a hardfaced layer thickness of approximately 1.5–2 mm.

Experiments with PrNl-3V14K were more limited. The available hardfacing material had a diameter of 5 mm, which was inconvenient for the equipment used during the industrial trials. As a result, only a small number of specimens were produced using this material, and they were not included in the microhardness measurements. In addition, the plant laboratory produced supplementary specimens by applying two hardfaced layers using Sv-08Cr20Ni9Mn7Ti wire. This material was not included in the numerical simulations and was used only as an additional series in the microhardness measurements, serving as a stainless-steel hardfacing reference.

After hardfacing, the selected specimens were sectioned, ground, polished, and prepared for metallographic examination. One transverse metallographic section was cut from each specimen using a water-cooled PBQ-5000Z metallographic cutting machine (Guangzhou Weiyi Metallographic Testing Instrument Co., Ltd., Guangzhou, China). Grinding and polishing were performed using a GP-2A grinding and polishing machine (Sinowon Innovation Metrology Manufacture Ltd., Dongguan, China). Grinding was performed sequentially using P400, P800, P1200, and P2500 abrasive papers. Polishing was carried out on a cloth wheel using PD-WT polycrystalline diamond suspensions with particle sizes of 1 and 0.25 μm (Trojan Material Technology Co., Suzhou, China). The microstructures of the substrate and HAZ were revealed using a 10% solution of nitric acid in alcohol, whereas the hardfaced-layer microstructure was revealed using Kroll's reagent

after repolishing. The hardfaced layer, the HAZ, and the 09G2S steel substrate were examined, with particular attention paid to the transition between the deposited metal and the base metal. Optical microscopy was performed using an OLYMPUS BX53M microscope (Olympus, Tokyo, Japan) equipped with MPlanFL N 50×/0.80 and 100×/0.90 objectives. Scanning electron microscopy was also employed for a more detailed examination of the microstructure and transition regions using a TESCAN VEGA 4 scanning electron microscope (TESCAN GROUP, a.s., Brno, Czech Republic) in secondary-electron (SE) and backscattered-electron (BSE) modes.

Microhardness was measured as an additional experimental indicator of changes in material properties in the hardfaced specimens. Vickers microhardness (ISO 6507-1 [39]) was measured using an HVS-1MD-AXY semiautomatic microhardness tester (HUATEC Group Corporation, Beijing, China) under a load of 0.05 kgf (0.49 N) and a dwell time of 10 s. Six indentations were made on each metallographic section, with two indentations in each of three visually identified regions: the base metal, the fusion boundary visible under the microscope, and the hardfaced layer. Two metallographic sections (n = 2) were examined for each of the Np-65G, Stoodite 6M, and Sv-08Cr20Ni9Mn7Ti materials, resulting in four indentations per region. The four indentations reported for each region were nested within two metallographic sections and therefore were not treated as four independent experimental replicates. The microhardness results are reported descriptively to characterize the examined sections; no inferential statistical comparison among the hardfacing materials was performed. The microhardness results are reported descriptively as mean values, standard deviations, medians, and ranges. The individual indentation values form part of the dataset available from the corresponding author upon reasonable request, as stated in the Data Availability Statement. A detailed analysis of the microstructure and chemical composition is beyond the scope of the present study and may be reported separately.

The experimental results characterize the microstructure and microhardness of hardfaced layers produced under industrial conditions. They do not provide a quantitative validation of the calculated thermal and mechanical fields, because thermal cycles, penetration depth, HAZ depth, residual stresses, and distortion were not measured.

Dilution, porosity, cracking, and fusion quality were not quantified in the experimental specimens. The presented micrographs are representative observations of the examined sections and cannot establish the absence, frequency, or spatial distribution of such defects. Consequently, the experimental results should be interpreted as a limited characterization of microstructure and microhardness rather than as a complete assessment of hardfacing quality.

3. Results

3.1. Numerical Response of the Hardfacing Process

The numerical results showed that the thermomechanical response of the 09G2S steel substrate changed with hardfacing current, arc voltage, travel speed, and preheating temperature. Nine simulations were carried out for each of the three hardfacing materials using the Taguchi L9 design.

All 27 simulations terminated normally. At the end of the simulation (1200 s), the maximum specimen temperatures ranged from 22 to 32 °C. The results of all simulations are presented in Table 4.

For each material, three of the nine conditions—Runs 2, 6, and 7—were found to be physically feasible. The conditions with the highest arc power P (Runs 3, 5, and 9) resulted in either a peak temperature above the boiling point of iron or a penetration depth exceeding 2 mm. The conditions with the lowest arc power (Runs 1, 4, and 8) resulted in either an unmelted central region of the bead or a penetration depth of less than 1 mm.

Table 4. Results of the 27 simulations: heat input $q = 3.6\eta UI/v$, peak temperature T_{max}, penetration depth h_p, HAZ depth beyond the fusion line h_{HAZ}, residual von Mises equivalent stress σeq (99th percentile), distortion δ, and equivalent plastic strain ε_p (99th percentile in the central region of the bead). Reasons for exclusion: B—boiling (T_{max} > 2861 °C); U—unmelted central region of the bead; P—penetration depth outside the range of 1.0–2.0 mm.

Material	Run	q, J/mm	T_{max}, °C	h_p, mm	h_{HAZ}, mm	σ_{eq} p99, MPa	δ, mm	ε_p p99	Status
Np-65G	1	1109	2037	0.74	3.86	279	0.101	0.032	U, P
Np-65G	2	1164	2587	1.76	4.71	300	0.149	0.039	feasible
Np-65G	3	1242	3148	2.34	4.76	303	0.171	0.041	B, P
Np-65G	4	798	2270	0.86	3.66	267	0.111	0.036	U, P
Np-65G	5	1811	2949	2.64	6.93	319	0.176	0.050	B, P
Np-65G	6	1109	2497	1.60	4.68	285	0.141	0.038	selected
Np-65G	7	1164	2593	1.80	4.77	302	0.148	0.039	feasible
Np-65G	8	776	2222	0.77	3.30	264	0.107	0.035	U, P
Np-65G	9	1774	2913	2.57	6.93	316	0.175	0.047	B, P
Stoodite 6M	1	1109	1973	0.68	3.76	324	0.175	0.059	U, P
Stoodite 6M	2	1164	2509	1.70	4.61	378	0.234	0.061	feasible
Stoodite 6M	3	1242	3058	BQ-5000Z 9	4.64	387	0.261	0.059	B, P
Stoodite 6M	4	798	2195	0.85	3.61	329	0.185	0.065	P
Stoodite 6M	5	1811	2891	2.61	6.86	393	0.286	0.066	B, P
Stoodite 6M	6	1109	2426	1.58	4.63	373	0.231	0.060	selected
Stoodite 6M	7	1164	2529	1.78	4.78	385	0.243	0.062	feasible
Stoodite 6M	8	776	2161	0.76	3.32	312	0.178	0.063	P
Stoodite 6M	9	1774	2848	2.55	6.91	391	0.280	0.064	P
PrNl-3V14K	1	610	2533	0.95	3.37	293	0.201	0.064	P
PrNl-3V14K	2	624	2676	1.43	3.48	289	0.209	0.062	selected
PrNl-3V14K	3	647	3092	1.78	3.86	277	0.203	0.057	B
PrNl-3V14K	4	462	2380	0.81	3.06	309	0.168	0.069	P
PrNl-3V14K	5	873	3298	2.10	4.11	311	0.223	0.056	B, P
PrNl-3V14K	6	610	2638	1.41	3.58	290	0.207	0.062	feasible
PrNl-3V14K	7	621	2688	1.52	3.72	291	0.201	0.058	feasible
PrNl-3V14K	8	457	2377	0.83	3.17	309	0.169	0.067	P
PrNl-3V14K	9	866	3286	2.12	4.20	315	0.220	0.053	B, P

The different responses did not change uniformly with variations in the process parameters. The conditions producing the lowest residual stresses—for example, Runs 4 and 8 for Np-65G, with values of 264–267 MPa—were physically infeasible because of insufficient penetration, whereas those producing the greatest penetration were excluded because of overheating. Therefore, the process conditions were compared using several responses rather than a single criterion.

The descriptive sum-of-squares analysis indicated that, within the investigated factor ranges, penetration depth was most sensitive to arc voltage (40–50%) and welding current (34–36%), followed by travel speed (14–25%). The estimated contribution of preheating temperature did not exceed 1%. For Np-65G and Stoodite 6M, HAZ depth was most sensitive to travel speed (44–45%), whereas residual stress was most sensitive to arc voltage (48–49%). These percentages are screening indicators and do not represent statistically tested effects.

Higher heat input generally produced higher peak temperatures and a wider thermally affected region. Thermal gradients and contraction during cooling also affected

stress and permanent deformation. These results indicate that the selection of a hardfacing condition should consider several thermomechanical responses together.

3.2. Hardfacing with Np-65G

The Np-65G simulations showed considerable variation between the investigated conditions. The peak temperature ranged from 2037 to 3148 °C, the penetration depth from 0.74 to 2.64 mm, the residual von Mises equivalent stress (99th percentile) from 264 to 319 MPa, the distortion from 0.10 to 0.18 mm, and the equivalent plastic strain (99th percentile) from 0.032 to 0.050.

Runs 1, 4, and 8, which had the lowest arc power, did not ensure complete melting of the central region of the bead: only 81–89% of the nodes exceeded the solidus temperature of the filler material. These runs also produced penetration depths of 0.74–0.86 mm. Although they exhibited the lowest residual stresses (264–279 MPa), fusion between the hardfaced layer and the substrate could not be ensured at such penetration depths. Runs 3, 5, and 9 produced peak temperatures of 2913–3148 °C and penetration depths of 2.3–2.6 mm. In Runs 5 and 9, performed at a travel speed of 3 m/h, the HAZ depth increased to 6.9 mm. Therefore, these runs were not considered the most favorable.

Run 6 provided the best combination of the evaluated parameters: a residual equivalent stress of 285 MPa, a HAZ depth of 4.68 mm, a penetration depth of 1.60 mm, a distortion of 0.14 mm, and an equivalent plastic strain of 0.038. The feasible Runs 2 and 7 produced residual stresses of 300–302 MPa at nearly the same HAZ depths of 4.71–4.77 mm. Run 6 was therefore selected as the most favorable Np-65G condition within the investigated parameter range. The distributions of residual von Mises equivalent stress, peak temperature, total displacement, and equivalent plastic strain obtained for the selected Run 6 condition are shown in Figure 3.

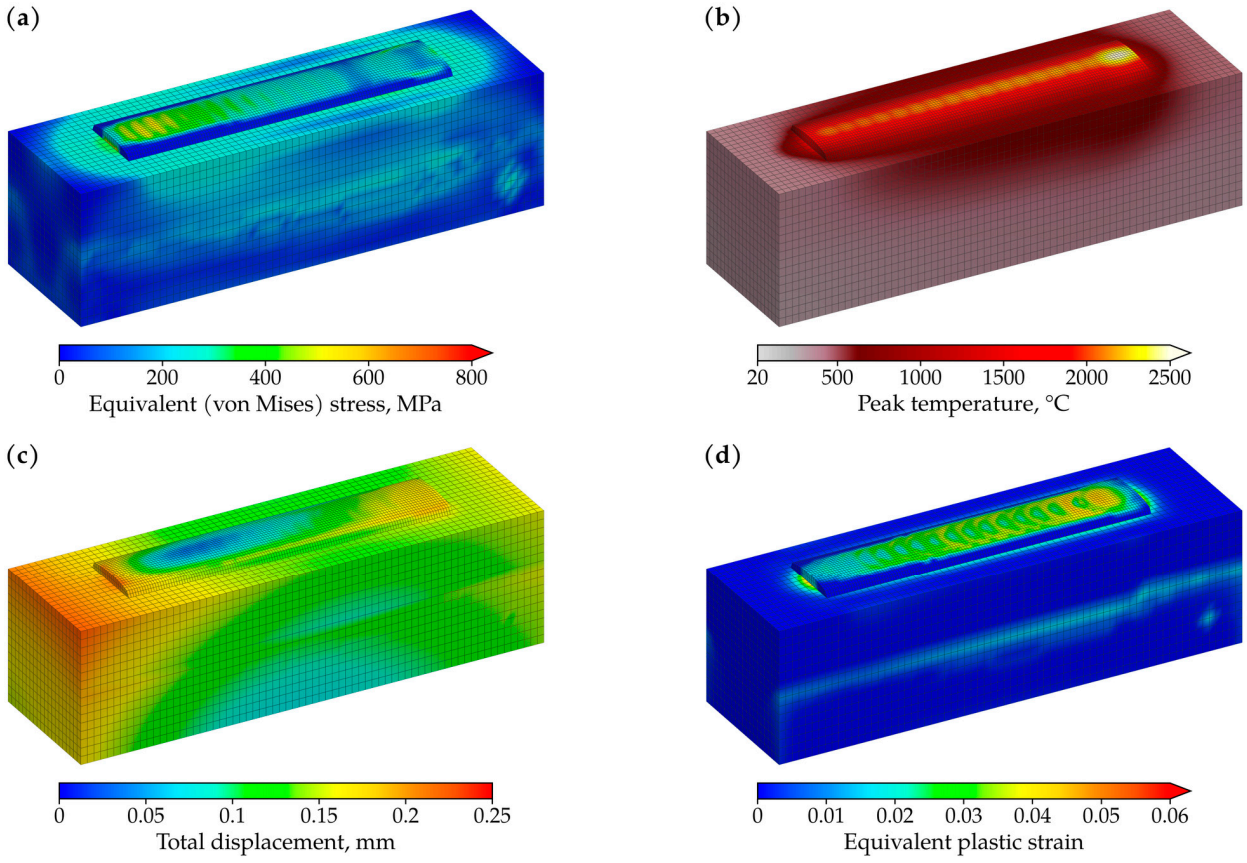


Figure 3. Results for the selected Np-65G condition (Run 6): (**a**) residual von Mises equivalent stress; (**b**) peak temperature; (**c**) total displacement; and (**d**) equivalent plastic strain.

The parameters for Run 6 were a preheating temperature of 190 °C, a current of 160 A, an arc voltage of 10 V, and a travel speed of 4 m/h.

The Np-65G results show that the lowest value of a single response does not necessarily correspond to the most suitable processing condition. In this case, the selected run provided a reasonable balance among penetration depth, equivalent stress, distortion, and HAZ depth.

3.3. Hardfacing with Stoodite 6M

The results for Stoodite 6M differed from those obtained for Np-65G. The residual von Mises equivalent stresses (99th percentile) ranged from 312 to 393 MPa and were therefore higher than those obtained for Np-65G, while the HAZ depth covered the same range of 3.3–6.9 mm. The distortion (0.18–0.29 mm) and equivalent plastic strain (0.059–0.066) were also greater than those obtained for Np-65G.

Run 6 provided the most favorable combination of the evaluated responses: a residual equivalent stress of 373 MPa, a HAZ depth of 4.63 mm, a penetration depth of 1.58 mm, a distortion of 0.23 mm, and an equivalent plastic strain of 0.060. Run 2 produced similar values (378 MPa and 4.61 mm, respectively), whereas Run 7 produced slightly higher values (385 MPa and 4.78 mm, respectively). Under the ranking criterion (Section 2.4), Run 6 had a lower residual stress than Run 2 at practically the same HAZ depth (4.63 versus 4.61 mm); its distortion (0.231 versus 0.234 mm) and equivalent plastic strain (0.060 versus 0.061) were also marginally lower, although these responses were not used in the ranking. Because the differences between the feasible runs did not exceed about 3%, Runs 2 and 6 can be regarded as practically equivalent.

Higher heat input generally resulted in a larger heat-affected region. Runs 5 and 9, performed at a travel speed of 3 m/h, produced a HAZ depth of approximately 6.9 mm, a penetration depth of approximately 2.6 mm, and the greatest distortion (0.28–0.29 mm). This indicates that increasing the heat input was not beneficial when the objective was to limit the thermal and mechanical effects on the 09G2S steel substrate.

Therefore, Run 6 was selected as the most favorable Stoodite 6M condition within the investigated range. Its parameters were a preheating temperature of 175 °C, a welding current of 160 A, an arc voltage of 10 V, and a travel speed of 4 m/h.

Compared with Np-65G at the same heat input, Stoodite 6M produced higher residual stresses (373 versus 285 MPa) and greater distortion (0.23 versus 0.14 mm), while the HAZ depths were nearly identical. Because the thermal conditions in the substrate were similar in both cases, the difference was primarily attributed to the properties of the deposited metal.

This does not mean that Stoodite 6M is necessarily the best hardfacing material for all applications. The numerical comparison considered mainly the thermomechanical response during deposition. The final material selection should also take into account the properties of the deposited layer, practical deposition conditions, wear resistance, cost, and compatibility with the available equipment.

3.4. Hardfacing with PrNl-3V14K

For PrNl-3V14K, the residual von Mises equivalent stresses (99th percentile) varied within a narrow range of 277–315 MPa. Greater variations were observed in penetration depth (0.81–2.12 mm) and peak temperature (2377–3298 °C), while the equivalent plastic strain (99th percentile) ranged from 0.053 to 0.069.

Runs 3, 5, and 9, which had the highest arc power, produced peak temperatures of 3092–3298 °C, exceeding the boiling point of iron. Run 3 nevertheless exhibited the lowest residual stress (277 MPa). Thus, the lower stress was accompanied by physically infeasible overheating. Runs 1, 4, and 8 produced penetration depths below 1 mm (0.81–0.95 mm).

Run 2 provided the most favorable combination of the evaluated responses: a residual equivalent stress of 289 MPa, a HAZ depth of 3.48 mm, a penetration depth of 1.43 mm, a distortion of 0.21 mm, and an equivalent plastic strain of 0.062. The feasible Runs 6 and 7 produced similar residual stresses (290–291 MPa) and slightly greater HAZ depths (3.58–3.72 mm). Run 2 therefore ranked first under the criterion described in Section 2.4, having both the lowest residual stress and the smallest HAZ depth among the feasible runs. Run 7 showed slightly lower distortion (0.201 versus 0.209 mm) and equivalent plastic strain (0.058 versus 0.062), but these responses were not part of the ranking criterion. The residual stresses of the three feasible runs differed by less than 1%, so they can be regarded as practically equivalent in this respect.

Run 2 was selected because it provided a more suitable balance than the runs with lower residual stresses but physically unacceptable overheating or penetration depth. Its parameters were a preheating temperature of 200 °C, a welding current of 180 A, an arc voltage of 12.5 V, and a travel speed of 10 m/h.

The results for PrNl-3V14K again demonstrate that the lowest residual stress does not always correspond to the most suitable hardfacing condition. In this case, reduced residual stress could be accompanied by overheating. Therefore, the selected run represents the most favorable balance among the evaluated responses within the investigated range.

3.5. Comparative Assessment and Selection of Processing Conditions

The results for the three materials showed that the thermomechanical response depended on both the processing parameters and the hardfacing material. The selected conditions are summarized in Table 5.

Table 5. Selected hardfacing process conditions based on the numerical assessment.

Material	Preheating Temperature, °C	Current, A	Voltage, V	Travel Speed, m/h	Selected Run
Np-65G	190	160	10	4	6
Stoodite 6M	175	160	10	4	6
PrNl-3V14K	200	180	12.5	10	2

The plots also enabled the HAZ depth and residual equivalent stress to be compared across all runs (Figure 4). For Np-65G and Stoodite 6M, residual stress and HAZ depth increased together, and the selected runs were located in the lower part of the feasible-run cluster. However, the runs with the lowest residual stresses and smallest HAZ depths were excluded because of insufficient penetration. For PrNl-3V14K, the residual stresses of the feasible runs were nearly identical (289–291 MPa), and the selection was therefore determined by HAZ depth. This demonstrates why both responses must be considered together with the penetration-depth constraint when selecting the process conditions.

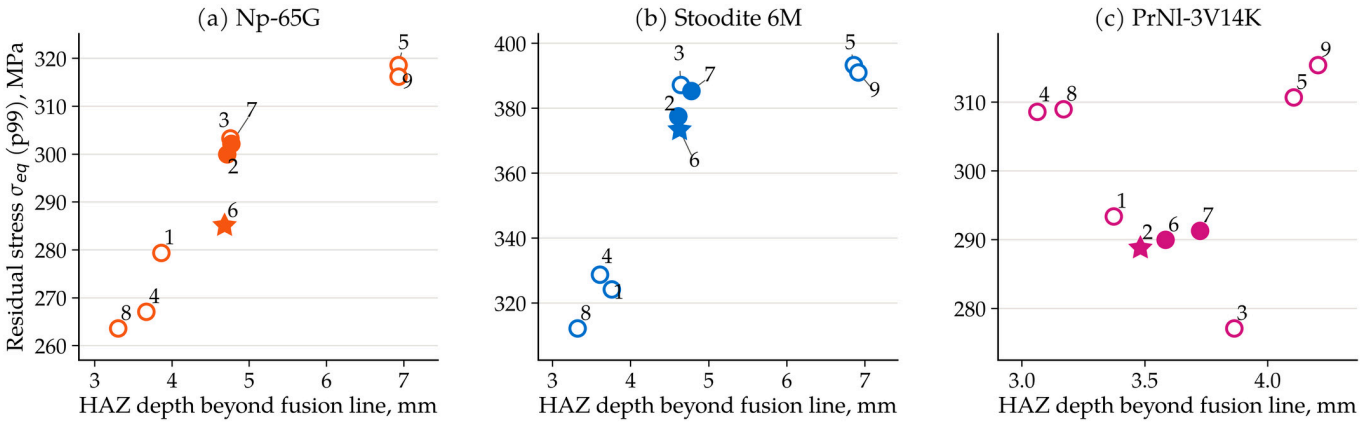
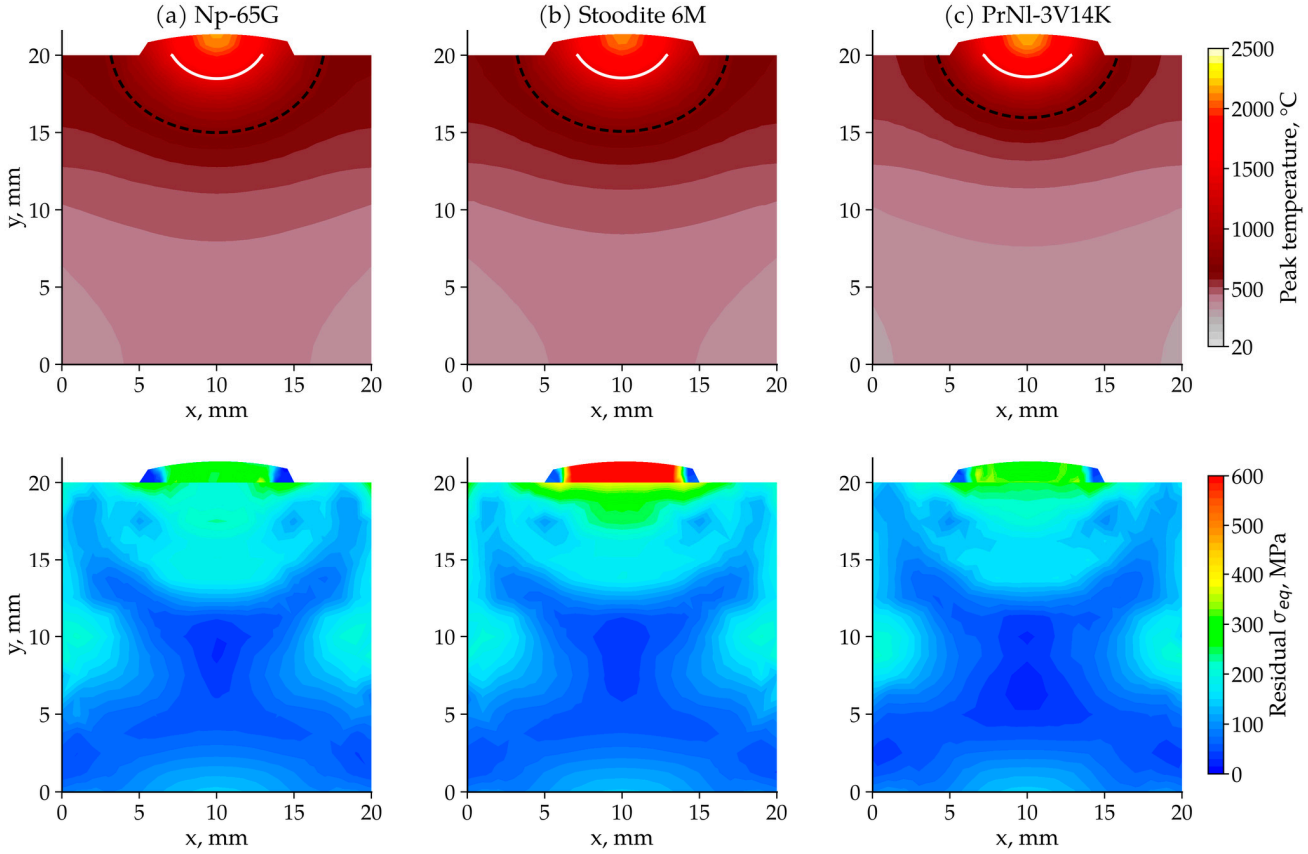


Figure 4. Relationship between HAZ depth beyond the fusion line and residual von Mises equivalent stress (99th percentile) for the investigated runs: (**a**) Np-65G; (**b**) Stoodite 6M; and (**c**) PrNl-3V14K. Filled circles indicate feasible runs (no boiling, at least 95% of the bead center melted, and a penetration depth of 1.0–2.0 mm); open circles indicate excluded runs; the star indicates the selected run; and the numbers indicate the L9 run numbers.

Transverse cross-sections of the specimens under the selected conditions are shown in Figure 5. For all three materials, the fusion line had a shallow bowl shape with a depth of 1.4–1.6 mm, while the A_{c1} = 725 °C isotherm beneath the center of the bead was located approximately 4–5 mm below the original substrate surface. The highest residual stresses were concentrated in the deposited bead and a thin subsurface layer of the substrate. In the remainder of the cross-section, they generally did not exceed 200 MPa and were approximately 100 MPa at its center. The highest stresses in the deposited bead were obtained for Stoodite 6M.



https://doi.org/10.3390/applmech7040098

Figure 5. Transverse cross-sections of the specimens under the selected conditions at the midpoint of the bead length (35 mm from the specimen end): (**a**) Np-65G; (**b**) Stoodite 6M; and (**c**) PrNl-3V14K. The upper row shows the peak temperature, and the lower row shows the residual von Mises equivalent stress. The *x*-axis represents the specimen width, and the *y*-axis represents the height measured from the bottom surface. The solid white line indicates 1460 °C (the solidus temperature of 09G2S steel and the fusion boundary), and the dashed black line indicates 725 °C (A_{c1} and the HAZ boundary).

The comparison shows that heat input had a strong influence on the thermomechanical response of the specimen. Welding current, arc voltage, travel speed, and preheating temperature acted jointly to determine the thermal conditions during hardfacing. Variations in these parameters affected residual stress, distortion, equivalent plastic strain, and HAZ depth.

Numerical simulation can thus identify parameter combinations associated with excessive thermal exposure before physical trials are performed. In the present study, it was used as a screening and parameter-selection tool.

3.6. Numerical Assessment of Gate Surface Restoration

After the simulations with rectangular specimens, the selected Np-65G condition was applied to a numerical model of the gate-valve working surface. Run 6 was used (preheating temperature of 190 °C, welding current of 160 A, arc voltage of 10 V, and travel speed of 4 m/h), with the same calibrated heat source and material cards as those used for the specimens. Np-65G was chosen for this check because it produced the lowest residual stresses among the three materials and is cobalt-free. Because a single gate-plate simulation required approximately 2 h of computing time on six cores, the selected condition was simulated only for Np-65G, whereas the adjusted condition described below was evaluated for Np-65G and Stoodite 6M, the two materials used in the industrial hardfacing trials. The component model was used to assess the transferability of the process conditions rather than to rank the hardfacing materials.

The gate-plate model (Figure 6) represented a 90-mm-thick 09G2S steel plate with overall dimensions of 1730 × 800 mm and a 700-mm-diameter through-hole. The region to be restored was an annular groove on the sealing surface beneath the seat, with a groove centerline radius of 300 mm. The groove cross-section was designed for a single bead, as in the specimen model: a bottom width of 10 mm, a depth of 1.36 mm, and sidewalls inclined at 30°. The bead filled the groove flush with the surface, corresponding to the condition after machining of the hardfaced layer; the machining operation itself was not modeled. Hardfacing was performed in a single pass over a length of 1885 mm, lasting approximately 28 min. The component was then cooled for 3 h, until its maximum temperature reached approximately 41 °C. The plate was constrained at the corners of its bottom surface using the 3-2-1 scheme. The thermal boundary conditions were the same as those used for the specimen model (Table 2). The plate was discretized into 103,000 tetrahedral elements, and the bead into 22,600 hexahedral elements.

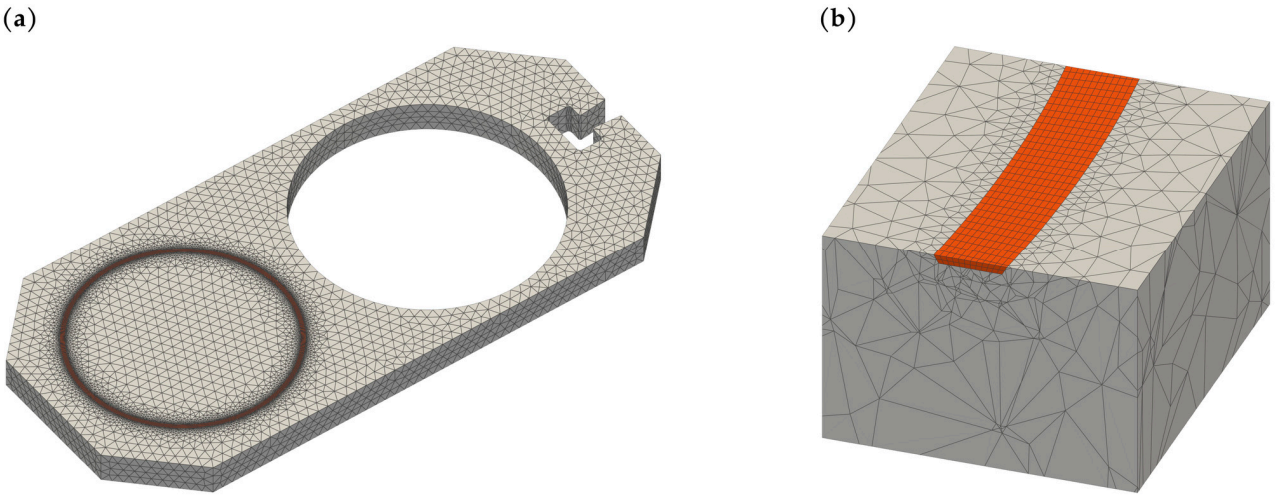


Figure 6. Numerical model of the gate plate with the region to be restored: (**a**) 09G2S steel plate with an annular groove on the sealing surface (radius of 300 mm) and the deposited bead (orange); (**b**) detail of the model near the groove, showing the bead filling the groove flush with the surface.

The results for the gate plate are presented in Figure 7 and Table 6 and compared with those obtained for the specimen under the same process conditions. The responses were determined in the same manner as for the specimen (Section 2.4) over the steady-state portion of the pass, corresponding to an angular range of 20–340° from the hardfacing start point.

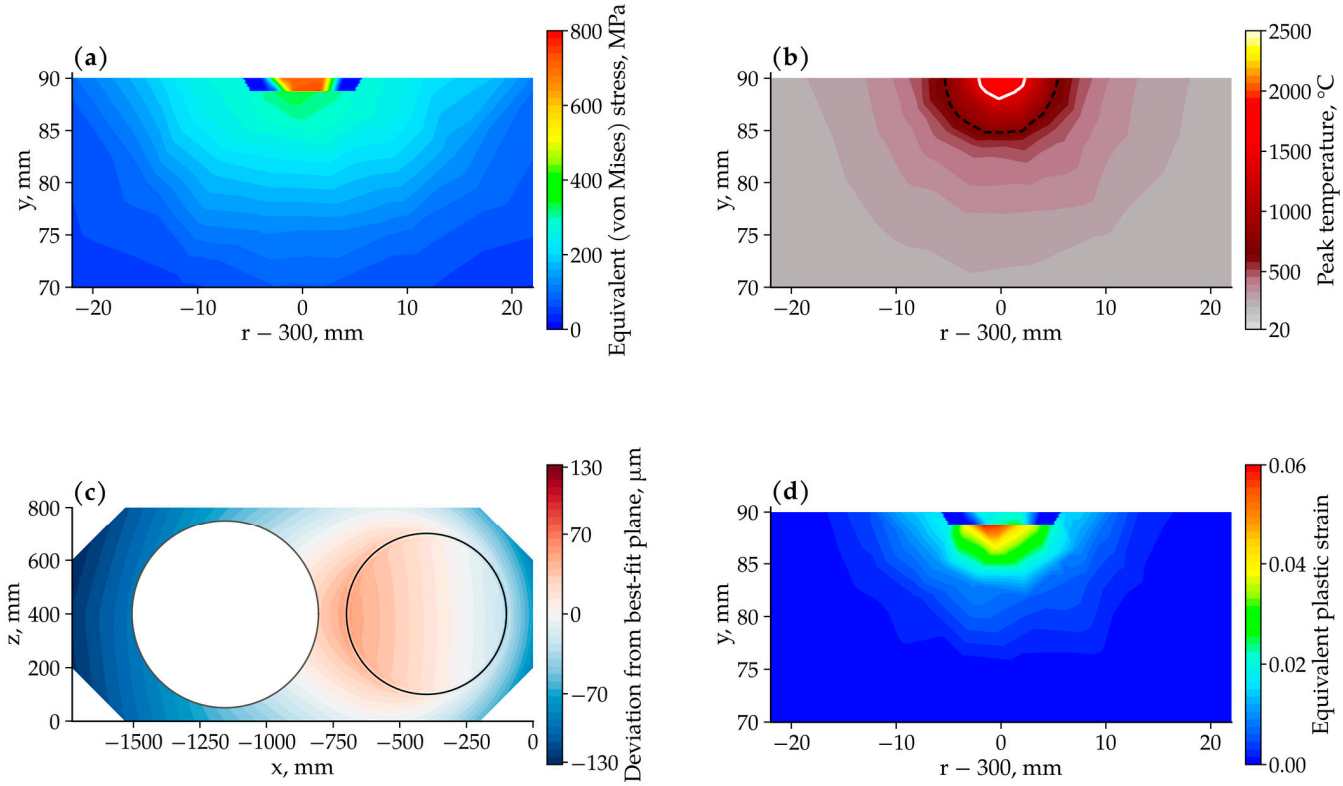


Figure 7. Thermomechanical response of the gate plate during simulated restoration using Np-65G under Run 6 conditions: (**a**) residual von Mises equivalent stress and (**b**) peak temperature in a radial cross-section of the ring (the solid white line indicates 1460 °C, corresponding to the fusion boundary; the dashed black line indicates 725 °C, corresponding to the HAZ boundary); (**c**) deviation of the sealing surface from the best-fit plane after cooling (the circle indicates the centerline of the hardfaced ring); and (**d**) equivalent plastic strain in the same cross-section.

https://doi.org/10.3390/applmech7040098

Table 6. Responses of the specimen and gate plate: selected Np-65G condition (Run 6) and adjusted condition (I = 160 A, U = 12 V, v = 3 m/h, T0 = 200 °C) for Np-65G and Stoodite 6M. Stress values represent the 99th percentile in the substrate within 15 mm of the surface and in the deposited bead.

Indicator	Specimen 20 × 20 × 70 mm	Gate, Np-65G, Run 6 (ring r = 300 mm)	Gate, Np-65G, Adjusted Condition	Gate, Stoodite 6M, Adjusted Condition
Peak substrate temperature, °C	2303	1724	2142	2118
Penetration, mm	1.60	≈0.5	1.63 (1.45–1.80)	1.62 (1.45–1.80)
Bead core melted, %	100	71	100	100
HAZ depth beyond the fusion line, mm	4.68	3.65 (max. 4.15)	4.35 (max. 5.00)	4.35 (max. 5.05)
σ_{eq} p99 in the substrate, MPa	301	346	346	358
σ_{eq} p99 in the deposited bead, MPa	403	764	790	1182
Equivalent plastic strain ε_P p99	0.038	0.060	0.061	0.069
Residual distortion δ, mm	0.14	0.15	0.22	0.24
Flatness deviation of the sealing surface, mm	—	0.19 (entire face); 0.03 (ring ± 30 mm)	0.28 (entire face); 0.06 (ring ± 30 mm)	0.31 (entire face); 0.07 (ring ± 30 mm)

The same process conditions as those used for the specimen produced substantially less heating in the gate plate. The peak substrate temperature decreased from 2303 to 1724 °C, the penetration depth decreased from 1.60 to approximately 0.5 mm, and only 71% of the central region of the bead was melted. The HAZ depth beyond the fusion line also decreased to 3.65 mm. According to the criteria defined in Section 2.4, these conditions are physically infeasible for the gate plate because the massive 90-mm-thick plate and the groove walls dissipate heat more effectively than the specimen with a 20 × 20 mm cross-section. The component will require a higher heat input, for example, by increasing the welding current or preheating temperature or by reducing the travel speed.

The residual stresses in the substrate near the ring were close to those obtained for the specimen (346 versus 301 MPa), whereas the stresses in the deposited bead were almost twice as high (764 versus 403 MPa). The bead confined within the groove of the massive component cannot contract freely during cooling, whereas the specimen can partially relieve the stresses through bending. The maximum stresses in the plate outside the deposited bead did not exceed 361 MPa.

Equivalent plastic strain remained concentrated primarily near the restored region (ε_P, 99th percentile = 0.060). This indicates that plastic deformation was localized around the region subjected to the thermal cycle.

After removing rigid-body motion and uniform shrinkage, the residual distortion of the component was 0.15 mm. The deviation of the sealing surface from the best-fit plane was 0.19 mm over the entire surface and 0.03 mm within the annular region extending ±30 mm from the bead centerline (Figure 7c). The drawing specifies a maximum flatness deviation of 0.2 mm for the sealing surfaces. For the original Run 6 component simulation, the calculated deviation of 0.19 mm over the entire face was slightly below the specified 0.2-mm value. This comparison does not apply to the adjusted higher-heat-input conditions discussed below. The total displacement of up to 3.1 mm was primarily associated with the uniform shrinkage of the plate as it cooled from the preheating temperature.

The gate-plate model demonstrated that the component geometry and boundary conditions affect the predicted thermomechanical response. Therefore, the results obtained using the simplified specimen should be interpreted with caution when transferred to the actual gate-plate geometry. In this case, applying the process conditions without modification resulted in insufficient penetration and higher residual stresses in the deposited metal.

To check whether a feasible condition exists for the gate plate within the investigated parameter levels, two additional simulations with an increased heat input were performed for Np-65G: I = 160 A, v = 3 m/h, T0 = 200 °C, and U = 14 or 12 V (q ≈ 2070 and 1770 J/mm, respectively). At 14 V, the penetration depth reached 2.0–2.4 mm and exceeded the upper limit of 2.0 mm. At 12 V (Table 6), the penetration depth was 1.45–1.80 mm (mean 1.63 mm), the bead core was fully melted, and the peak temperature (2283 °C in the bead) remained below the boiling point; this condition is therefore feasible according to the criteria of Section 2.4. With Stoodite 6M, the same condition gave practically the same penetration and HAZ depths, whereas the residual stress in the deposited bead was higher (1182 versus 790 MPa), consistent with the higher yield strength of the cobalt-based alloy. The increased heat input raised the residual distortion from 0.15 to 0.22–0.24 mm and the flatness deviation of the entire face from 0.19 to 0.28–0.31 mm, whereas the deviation within the sealing ring (±30 mm) remained 0.06–0.07 mm. The same parameter combination corresponds to Run 9 of the Np-65G L9 design, which caused boiling in the specimen (Table 4). A condition that is infeasible for a small specimen can therefore be feasible for the massive component, and the feasible window must be determined for the component itself.

Under the adjusted conditions, the calculated flatness deviation was 0.28–0.31 mm over the entire face and 0.06–0.07 mm within the annular region extending ±30 mm from the bead centerline. The model did not simulate material removal, stress redistribution, or final surface formation during machining. Therefore, compliance of the finished sealing surface with the specified 0.2-mm flatness tolerance cannot be established from the present simulation. The calculated values should be interpreted as indicators of the distortion produced by a single hardfacing pass, while final dimensional compliance must be assessed after the actual machining stage.

3.7. Experimental Characterization of Industrially Hardfaced Specimens

Specimens hardfaced under industrial conditions were examined to characterize the deposited layers.

The industrial hardfacing conditions were selected by an experienced welding specialist based on arc stability, weld-pool behavior, and bead quality and therefore did not exactly match the simulated conditions. The welding current, arc voltage, and preheating temperature were within the investigated ranges, whereas the travel speed and therefore the heat input differed (Section 2.5). For PrNl-3V14K, the industrial welding current (180 A) and preheating temperature (200 °C) matched those of the numerically selected Run 2, while its arc voltage of 12.5 V fell within the industrial range of 11–14 V.

For this reason, the experimental results are used to characterize the hardfaced layers and are not treated as a validation of the numerical model.

Metallographic examination showed three main regions in the hardfaced specimens: the deposited layer, the heat-affected zone, and the 09G2S substrate. A transition region between the deposited material and the substrate was visible in the prepared cross-sections.

Optical and scanning electron microscopy revealed distinct structural regions corresponding to the deposited layer, HAZ, and base material, as illustrated in Figure 8.

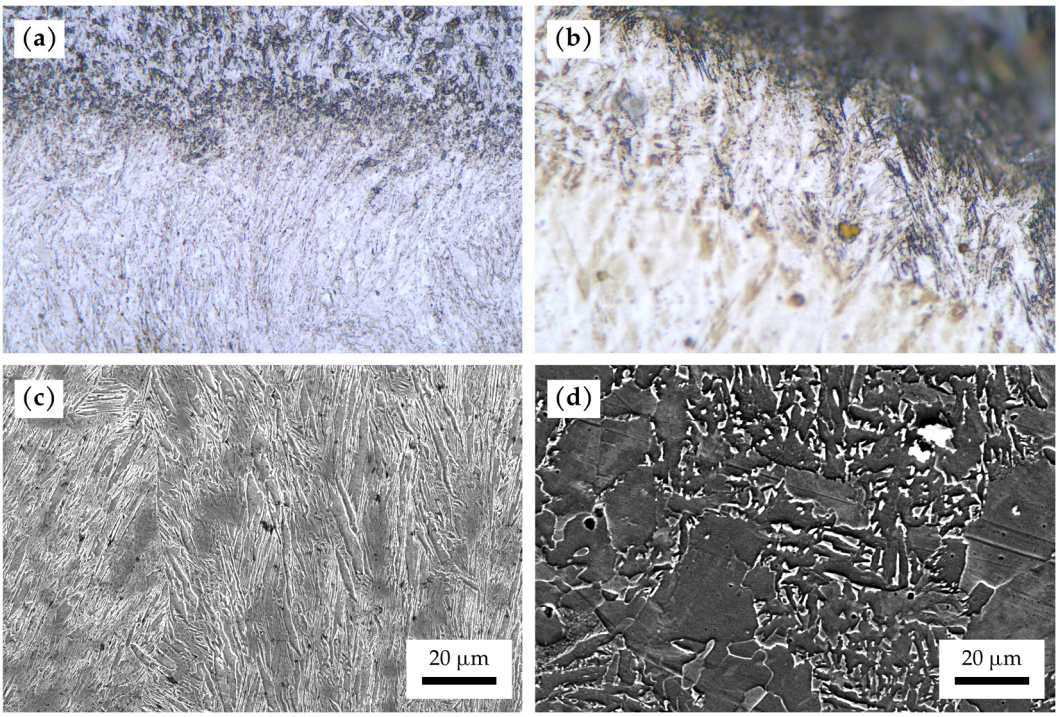


Figure 8. Representative microstructures of experimentally hardfaced 09G2S steel specimens: (**a**) optical micrograph of the transition region in a specimen hardfaced with Stoodite 6M; (**b**) optical micrograph of the transition region in a specimen hardfaced with Sv-08Cr20Ni9Mn7Ti; (**c**) secondary-electron (SE) SEM image of a specimen hardfaced with Stoodite 6M; and (**d**) secondary-electron (SE) SEM image of the HAZ in a specimen hardfaced with Sv-08Cr20Ni9Mn7Ti. Optical micrographs were obtained using a 100× objective.

The measured microhardness values are summarized in Figure 9 and Table 7. In the examined sections, the median values increased from 214–257 HV0.05 in the base metal to 299–350 HV0.05 at the fusion boundary and 384–481 HV0.05 in the hardfaced layer. Because only two metallographic sections were examined for each material and the four indentations per region were nested within these sections, the results are treated as descriptive observations. They are not used for inferential statistical comparisons among the hardfacing materials or for validation of the numerical model.

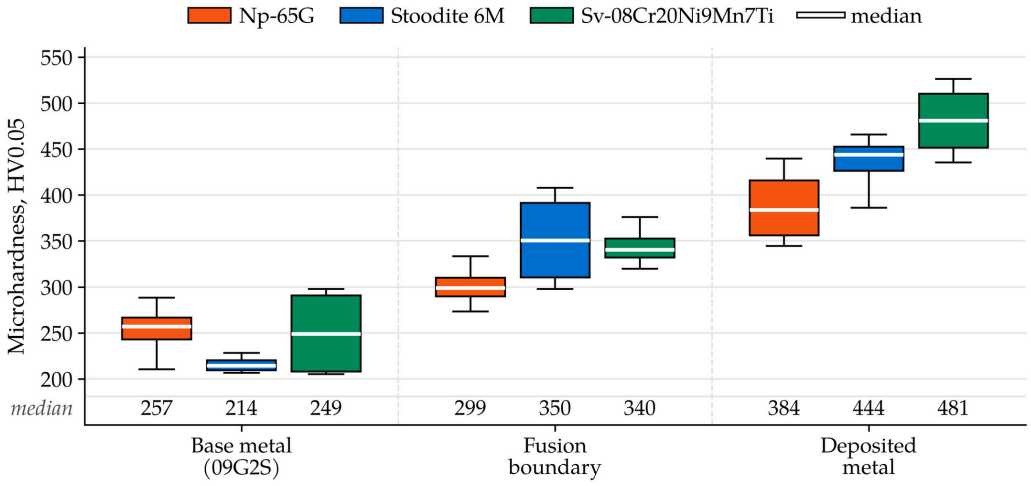


Figure 9. Distribution of microhardness across the regions of the hardfaced specimens: base metal (09G2S), fusion boundary, and deposited metal. For each material, two metallographic sections were

examined, with two indentations per region on each section (four values per box). The boxes represent the interquartile range, the white lines indicate the medians, and the whiskers indicate the minimum and maximum values; the numbers below the boxes are the median values. Sv-08Cr20Ni9Mn7Ti represents an additional experimental series (Section 2.5).

Table 7. Descriptive microhardness values (HV0.05) for the examined regions, reported as mean ± standard deviation (median; minimum–maximum). For each material, four indentations per region were nested within two metallographic sections.

Material	Base Metal	Fusion Boundary	Hardfaced Layer
Np-65G	253 ± 32 (257; 211–288)	301 ± 25 (299; 273–333)	388 ± 44 (384; 345–440)
Stoodite 6M	216 ± 10 (214; 206–228)	352 ± 54 (350; 298–408)	435 ± 34 (444; 386–466)
Sv-08Cr20Ni9Mn7Ti	250 ± 50 (249; 205–298)	344 ± 24 (340; 320–376)	481 ± 42 (481; 435–526)

In the examined sections, the Stoodite 6M hardfaced layer showed a median microhardness of 444 HV0.05 and a range of 386–466 HV0.05, whereas the Np-65G hardfaced layer showed a median of 384 HV0.05 and a range of 345–440 HV0.05. These observations characterize the examined specimens but do not establish a statistically generalizable difference between the two hardfacing materials. The additional Sv-08Cr20Ni9Mn7Ti series showed a median of 481 HV0.05 and a range of 435–526 HV0.05; this series was included only as an experimental reference and was not modeled numerically.

A comparison of Stoodite 6M and Np-65G shows that the numerical and experimental results provide different but complementary information. Under the selected conditions, Stoodite 6M produced higher residual stresses and greater distortion than Np-65G in the numerical model. In the examined sections, the observed median and range of microhardness were higher for the Stoodite 6M hardfaced layer than for the Np-65G layer; however, the limited number of sections does not support a statistically generalizable comparison between the materials. However, the selection of a hardfacing material should also consider its composition, wear resistance, hardfacing process stability, availability, and cost. These factors were not investigated in detail in the present study.

The trials with PrNl-3V14K also revealed a practical limitation that was not apparent from the numerical simulations. The available 5-mm-diameter rod was inconvenient for use with the equipment employed in the industrial hardfacing trials. Consequently, only a limited number of specimens could be produced. This example demonstrates why numerical results must be considered together with practical manufacturing conditions.

3.8. Implications and Limitations of Numerical Screening and Experimental Characterization

The numerical screening and the experimental characterization provide complementary but not directly comparable information. The numerical model describes the relative thermomechanical response of the investigated conditions, whereas the experiments characterize the microstructure and microhardness of separately produced industrial specimens.

The numerical analysis enabled 27 process conditions to be compared in terms of residual stress, distortion, equivalent plastic strain, peak temperature, and HAZ depth and allowed physically infeasible conditions to be excluded. The experimental part of the study was limited to the characterization of hardfaced layers.

Several limitations of the present study should be noted. First, the heat source was calibrated against a theoretical penetration depth rather than measured thermal cycles or weld-pool geometry. Second, the properties of the hardfacing materials were specified using standards and technical data sheets for analogous alloy grades, and phase transformations were not modeled. Therefore, the model does not predict hardness or phase composition. To estimate the effect of this simplification, the industrial conditions (I = 140 A,

U = 11 V, v = 4 m/h) were additionally simulated with the multiphase S355J2G3 material model from the Simufact database (phase transformations based on CCT/TTT data) for the substrate. Compared with the single-phase 09G2S model, the 99th-percentile residual stress increased from 275 to 377 MPa for Np-65G and from 366 to 436 MPa for Stoodite 6M; the penetration depth increased by about 0.16 mm, the HAZ depth changed by up to 0.55 mm, and the distortion changed by less than 0.01 mm. This comparison does not isolate the effect of phase transformations because the substrate material card was changed from 09G2S to the available multiphase S355J2G3 model. It is therefore used only to illustrate the possible sensitivity of the predicted residual stresses to the substrate constitutive description. It does not constitute validation of the phase-transformation behavior of 09G2S. Third, the L9 design is saturated, and factor interactions cannot be separated from the main effects. Fourth, the industrial hardfacing conditions, in particular the travel speed and therefore the heat input, differed from the simulated conditions; thermal cycles, penetration depth, dilution, HAZ depth, residual stresses, distortion, porosity, cracking, and fusion quality were not measured or quantitatively evaluated; and only a small number of metallographic sections were examined (n = 2 per material). Fifth, the gate-plate model considered only a single pass, and machining of the hardfaced layer was not modeled. Sixth, the substrate was discretized with 1 mm elements. To quantify the mesh effect, the three selected conditions were recalculated with a refined substrate mesh (0.5 × 0.5 mm in plan and 0.5 mm in the upper 6 mm; 128,800 instead of 22,400 elements). The section-averaged HAZ depth changed by less than 1.5%, the 90th-percentile penetration depth by less than 2.5%, the residual stress by 2.5–6.5%, and the distortion by less than 3%, while the maximum penetration depth increased by 2–9% (0.04–0.14 mm) and the bead core was fully melted with both meshes. The largest single-section HAZ depth was sensitive to the node positions near the end of the evaluation window, with a change of up to 36% for PrNl-3V14K, whereas within x = 21–49 mm the change was less than 4.5%. This sensitivity indicates that the exact maximum HAZ depth and the local position of the calculated thermal boundaries should not be interpreted as mesh-independent predictions. The mesh-refinement results nevertheless showed substantially smaller changes in the section-averaged HAZ depth, penetration-depth percentile, residual stress, and distortion. Accordingly, the model is used for comparative screening of the investigated conditions rather than for precise prediction of the local fusion-boundary or HAZ geometry. Consequently, the experimental results characterize the hardfaced layers but do not validate the predicted thermal and mechanical fields. In contrast, previous studies have directly compared numerical thermal and mechanical results with experimental measurements [23,24]. Direct measurements of residual stresses in Stellite hardfaced layers have also been reported [40–42]; comparison of the predicted values with these measurements may represent the next step in model validation.

Despite these limitations, the numerical model was used for preliminary screening of the investigated process conditions. Parameter combinations associated with metal boiling, insufficient penetration, high residual stress, large distortion, or a deep HAZ can be identified before industrial trials. Experimental hardfacing can then be focused on a narrower range of process conditions.

This is important for gate-valve restoration because excessive heat input may affect both the hardfaced layer and the geometry of the component. Numerical screening and industrial specimen characterization can be used as complementary stages when developing a hardfacing procedure. In the present study, however, the experimental observations were not used for quantitative validation of the predicted thermal or mechanical fields.

4. Conclusions

This study investigated numerically the hardfacing process parameters for the restoration of gate-valve components made of 09G2S steel and characterized specimens hardfaced under industrial conditions. Simulations were carried out in Simufact Welding using a Taguchi L9 design. Welding current, arc voltage, travel speed, and preheating temperature were varied for three hardfacing materials: Np-65G, Stoodite 6M, and PrNl-3V14K. A total of 27 simulated conditions were compared in terms of von Mises equivalent stress, distortion, equivalent plastic strain, temperature response, penetration depth, and HAZ depth.

The Goldak heat source was calibrated against a theoretical penetration depth of 1.2–1.5 mm, and a single set of heat-source parameters was found to be suitable for all three materials. After screening for physical feasibility—no metal boiling, a melted central region of the bead, and a penetration depth of 1.0–2.0 mm—three of the nine conditions were found to be feasible for each material.

The results showed that a hardfacing condition could not be selected on the basis of a single response. The lowest residual stresses were obtained under conditions associated with either insufficient penetration or overheating. Therefore, the process conditions were selected by considering several thermomechanical responses simultaneously.

Within the investigated parameter ranges, the following conditions gave the most favorable overall results:

- Np-65G: Run 6—preheating temperature 190 °C, current 160 A, arc voltage 10 V, and travel speed 4 m/h;
- Stoodite 6M: Run 6—preheating temperature 175 °C, current 160 A, arc voltage 10 V, and travel speed 4 m/h;
- PrNl-3V14K: Run 2—preheating temperature 200 °C, current 180 A, arc voltage 12.5 V, and travel speed 10 m/h.

The descriptive factor-sensitivity analysis indicated that, within the investigated ranges, penetration depth was most responsive to arc voltage and welding current. Because the L9 design was saturated and contained no replicated simulations, these results should be interpreted as screening indicators rather than statistically confirmed factor effects. At comparable heat inputs, Stoodite 6M produced higher residual stresses (373 versus 285 MPa) and greater distortion than Np-65G. In the examined metallographic sections, the observed microhardness values of the Stoodite 6M hardfaced layer ranged from 386 to 466 HV0.05, whereas those of the Np-65G layer ranged from 345 to 440 HV0.05. Because only two sections were examined per material, these results provide a descriptive characterization and should not be interpreted as a statistically established difference between the materials. However, the thermomechanical results and microhardness values alone are insufficient for the final selection of a hardfacing material. Hardfacing stability, material availability, equipment compatibility, wear resistance, and the required properties of the restored surface must also be considered.

The selected Np-65G condition was also applied to a numerical model of the gate plate. Under the same conditions, the gate-plate model produced a penetration depth of approximately 0.5 mm instead of 1.60 mm and incomplete melting of the bead, while the residual stress in the deposited metal increased from 403 to 764 MPa. The residual stress in the substrate changed only slightly (346 versus 301 MPa). The flatness deviation of the sealing surface after a single pass was 0.19 mm. The difference from the rectangular specimen demonstrates that component geometry and boundary conditions affect the predicted stress and deformation fields. Therefore, parameter combinations selected using simplified specimens should be reassessed when transferred to the actual component geometry. The gate plate requires a higher heat input than the specimen: an adjusted condition within the investigated levels (160 A, 12 V, 3 m/h, 200 °C) gave a penetration depth of 1.45–1.80 mm and a fully melted bead for both Np-65G and Stoodite 6M, at the cost of

larger distortion (0.22–0.24 mm). The same condition caused boiling in the specimen, so the feasible window must be determined for the component itself.

The specimens hardfaced under industrial conditions showed microhardness increasing from the base metal to the deposited layer. Because the industrial travel speed and heat input differed from the simulated conditions and the thermal and mechanical responses were not measured, the experimental results characterize the hardfaced layers but do not validate the numerical model.

Numerical simulation provided a means of preliminary screening of hardfacing conditions and for identifying parameter combinations associated with high residual stress, large distortion, or a deep HAZ before industrial trials. This approach may reduce the number of physical trials required when developing a hardfacing procedure.

Further work should include direct measurements of thermal cycles, penetration depth, dilution, HAZ dimensions, and distortion, together with quantitative evaluation of fusion quality, porosity, and cracking. The heat-source model should also be refined and calibrated using experimental data, and the numerical model should be extended to include phase transformations. Wear testing of the hardfaced layers would provide additional information for assessing the long-term performance of restored gate-valve components.

Author Contributions: Conceptualization, R.G., S.B. and K.S.; methodology, R.G., D.Z. and A.M.; formal analysis, R.G., S.B. and T.B.; investigation, D.Z., S.B. and K.S.; data curation, D.Z., A.M. and T.B.; visualization, R.G., A.M. and T.B.; writing—original draft preparation, R.G., D.Z. and S.B.; writing—review and editing, K.S., A.M. and T.B.; supervision, K.S., A.M. and T.B.; project administration, D.Z., S.B. and K.S. All authors have read and agreed to the published version of the manuscript.

Funding: This research was funded by the Science Committee of the Ministry of Science and Higher Education of the Republic of Kazakhstan (grant no. AP22683698).

Institutional Review Board Statement: Not applicable.

Informed Consent Statement: Not applicable.

Data Availability Statement: The datasets generated and analyzed during the current study are available from the corresponding author upon reasonable request.

Acknowledgments: The authors sincerely thank the anonymous reviewers for their careful evaluation and insightful comments, which have substantially enhanced the quality and clarity of the manuscript.

Conflicts of Interest: The authors declare no conflicts of interest.

References

1. Klimpel, A.; Dobrzański, L.A.; Lisiecki, A.; Janicki, D. The study of the technology of laser and plasma surfacing of engine valves face made of X40CrSiMo10-2 steel using cobalt-based powders. *J. Mater. Process. Technol.* **2006**, *175*, 251–256. https://doi.org/10.1016/j.jmatprotec.2005.04.050.
2. Yu, Q.; Zhang, W.; Shang, J.; Liu, B.; Pei, Y.; Li, Y.; Ao, S. Comparative investigation on the microstructure and corrosion properties of surfacing cobalt alloys by various methods. *Surf. Coat. Technol.* **2024**, *494*, 131386. https://doi.org/10.1016/j.surfcoat.2024.131386.
3. Fu, J.; Gui, W.; Qin, J.; Lin, J.; Ren, X.; Luan, B. High-speed laser-clad 3533-00 Fe-based cemented carbide coatings on nuclear power valve sealing surface to enhanced wear and corrosion resistance. *Surf. Coat. Technol.* **2024**, *480*, 130594. https://doi.org/10.1016/j.surfcoat.2024.130594.
4. Ding, Y.; Liu, R.; Yao, J.; Zhang, Q.; Wang, L. Stellite alloy mixture hardfacing via laser cladding for control valve seat sealing surfaces. *Surf. Coat. Technol.* **2017**, *329*, 97–108. https://doi.org/10.1016/j.surfcoat.2017.09.018.

5. Que, Z.; Ahonen, M.; Virkkunen, I.; Nevasmaa, P.; Rautala, P.; Reinvall, H. Study of cracking and microstructure in Co-free valve seat hardfacing. *Nucl. Mater. Energy* **2022**, *31*, 101202. https://doi.org/10.1016/j.nme.2022.101202.
6. Mussina, Z.; Iskakova, D.; Kassenov, A.; Abishev, K.; Itybayeva, G.; Taskarina, A.; Suleimenov, A.; Mazdubay, A.; Nurkimbayev, S.; Radjibaev, D. An experimental study of the tribological properties of a wedge gate valve components with Sv-10Kh17T welding wire surfacing. *Eng. Technol. Appl. Sci. Res.* **2025**, *15*, 28891–28897. https://doi.org/10.48084/etasr.13453.
7. Gabdyssalyk, R.; Kombayev, K.; Kilymbekov, N.; Kapkenova, M.; Kapaeva, S. Effect of TIG hardfacing process parameters on the structural characteristics of shut-off valve components. *EKTU J. Eng. Sci.* **2026**, *1*, JES_3_2026. https://doi.org/10.51885/3134-8009_jes_2026_3_9.
8. Sachajdak, A.; Słoma, J.; Szczygieł, I. Thermal model of the Gas Metal Arc Welding hardfacing process. *Appl. Therm. Eng.* **2018**, *141*, 378–385. https://doi.org/10.1016/j.applthermaleng.2018.05.120.
9. Guo, H.; Fan, C.; Yang, S.; Wang, J.; Pei, W.; Chu, Z. Numerical simulation of layered bimetallic ZChSnSb8Cu4/steel TIG-MIG hybrid welding based on Simufact. *Materials* **2023**, *16*, 5346. https://doi.org/10.3390/ma16155346.
10. Wei, B.; Liu, Z.; Xu, M.; Hong, Y.; Zhu, D. Numerical simulation of efficient welding for thick plates in shipbuilding using Simufact Welding. *J. Phys. Conf. Ser.* **2024**, *2760*, 012050. https://doi.org/10.1088/1742-6596/2760/1/012050.
11. da Silva, L.O.P.; Lima, T.N.; dos Santos Júnior, F.M.; Callegari, B.; Folle, L.F.; Coelho, R.S. Heat-affected zone microstructural study via coupled numerical/physical simulation in welded superduplex stainless steels. *Crystals* **2024**, *14*, 204. https://doi.org/10.3390/cryst14030204.
12. Li, C.; Liu, Y.; Luo, F.; Han, X.; Feng, L. Multi-field coupling numerical simulation and experimental research of submerged arc surfacing process on the descaling rolls with different wall thickness. *J. Adhes. Sci. Technol.* **2024**, *38*, 3144–3178. https://doi.org/10.1080/01694243.2024.2329384.
13. Bararpour, S.M.; Jamshidi Aval, H.; Jamaati, R. Modeling and experimental investigation on friction surfacing of aluminum alloys. *J. Alloys Compd.* **2019**, *805*, 57–68. https://doi.org/10.1016/j.jallcom.2019.07.010.
14. Aminzadeh, A.; Sattarpanah Karganroudi, S.; Goldak, J. Insight into the key process parameters on residual stress distribution in deep drawing of laser-welded blanks: Response surface modeling. *J. Mater. Eng. Perform.* **2024**, *33*, 4136–4148. https://doi.org/10.1007/s11665-024-09286-w.
15. Tian, L.; Xing, S.; Liu, G.; Luo, Y. Numerical simulation of hardfacing remanufacturing for large-scale damaged grinding roller. *Int. J. Adv. Manuf. Technol.* **2021**, *118*, 2613–2649. https://doi.org/10.1007/s00170-021-08073-4.
16. Kaszuba, M.; Lachowicz, M.; Widomski, P.; Kustroń, P.; Rzadkosz, T.; Sokołowski, P.; Gronostajski, Z. Application of Numerical Modeling to Determine the Parameters of the Hardfacing Process and to Determine the Properties of the Obtained Hardfacing Layers of Forging Dies. *Arch. Metall. Mater.* **2026**, *71*, 923–932. https://doi.org/10.24425/amm.2026.1984.
17. Nurzhanova, O.; Zharkevich, O.; Bessonov, A.; Naboko, Y.; Abdugaliyeva, G.; Taimanova, G.; Nikonova, T. Simulation of the distribution of temperature, stresses and deformations during splined shafts hardfacing. *J. Appl. Eng. Sci.* **2023**, *21*, 837–845. https://doi.org/10.5937/jaes0-42774.
18. Goldak, J.; Chakravarti, A.; Bibby, M. A new finite element model for welding heat sources. *Metall. Trans. B* **1984**, *15*, 299–305. https://doi.org/10.1007/BF02667333.
19. Yang, Q.-X.; Yao, M.; Park, J.-K. Numerical simulations and measurements of temperature and stress field in medium-high carbon steel specimen after hard-face-welding. *Comput. Mater. Sci.* **2004**, *29*, 37–42. https://doi.org/10.1016/S0927-0256(03)00093-4.
20. Yang, Q.-X.; Yao, M.; Park, J.-K. Numerical simulation on residual stress distribution of hard-face-welded steel specimens with martensite transformation. *Mater. Sci. Eng. A* **2004**, *364*, 244–248. https://doi.org/10.1016/j.msea.2003.08.024.
21. Joshi, S.; Hildebrand, J.; Aloraier, A.S.; Rabczuk, T. Characterization of material properties and heat source parameters in welding simulation of two overlapping beads on a substrate plate. *Comput. Mater. Sci.* **2013**, *69*, 559–565. https://doi.org/10.1016/j.commatsci.2012.11.029.
22. Jafarzadegan, M.; Taghiabadi, R.; Mofid, M.A. Using double ellipsoid heat source model for prediction of HAZ grain growth in GTAW of stainless steel 304. Mater. *Today Commun.* **2022**, *31*, 103411. https://doi.org/10.1016/j.mtcomm.2022.103411.
23. Chiocca, A.; Frendo, F.; Bertini, L. Evaluation of residual stresses in a pipe-to-plate welded joint by means of uncoupled thermal-structural simulation and experimental tests. *Int. J. Mech. Sci.* **2021**, *199*, 106401. https://doi.org/10.1016/j.ijmecsci.2021.106401.
24. Jia, Y.; Saadlaoui, Y.; Hamdi, H.; Sijobert, J.; Roux, J.-C.; Bergheau, J.-M. An experimental and numerical case study of thermal and mechanical consequences induced by laser welding process. *Case Stud. Therm. Eng.* **2022**, *39*, 102414. https://doi.org/10.1016/j.csite.2022.102414.

25. *GOST 34233.1-2017*. Vessels and Apparatus. Norms and Methods of Strength Calculation. General Requirements; Standartinform: Moscow, Russia, 2018.
26. *EN 1993-1-2:2005*. Eurocode 3: Design of Steel Structures—Part 1–2: General Rules—Structural Fire Design; CEN: Brussels, Belgium, 2005.
27. Sugden, A.A.B.; Bhadeshia, H.K.D.H. Thermodynamic estimation of liquidus, solidus, Ae3 temperatures, and phase compositions for low alloy multicomponent steels. *Mater. Sci. Technol.* **1989**, *5*, 977–984. https://doi.org/10.1179/mst.1989.5.10.977.
28. Deloro. Stellite 6 Alloy: Material Data Sheet. Available online: https://www.deloro.com/wp-content/uploads/2025/05/Deloro_MDS_Stellite6_rev00.pdf (accessed on 11 October 2026).
29. HTS Coatings. Stellite 1: Material Properties. Available online: https://htscoatings.com/coatings/stellite-1 (accessed on 11 October 2026).
30. Stenbacka, N. On arc efficiency in gas tungsten arc welding. *Soldag. Insp.* **2013**, *18*, 380–390. https://doi.org/10.1590/S0104-92242013000400010.
31. Goldak, J.A.; Akhlaghi, M. *Computational Welding Mechanics*; Springer: New York, NY, USA, 2005. https://doi.org/10.1007/b101137.
32. Mihaylov, O. Determining the positions of the elements for the 3-2-1 principle of location in a SolidWorks add-in. In Proceedings of the 12th International Scientific and Practical Conference "Environment. Technology. Resources", Rezekne, Latvia, 20–22 June 2019; Volume 3, pp. 160–165. https://doi.org/10.17770/etr2019vol3.4138.
33. Roy, R.K. *Design of Experiments Using the Taguchi Approach: 16 Steps to Product and Process Improvement*; Wiley: New York, NY, USA, 2001; ISBN 978-0-471-36101-5.
34. NIST/SEMATECH. e-Handbook of Statistical Methods, Section 5.3.3.10: Three-Level, Mixed-Level and Fractional Factorial Designs. Available online: https://www.itl.nist.gov/div898/handbook/pri/section3/pri33a.htm (accessed on 11 October 2026).
35. Trzaska, J. Calculation of Critical Temperatures by Empirical Formulae. *Arch. Metall. Mater.* **2016**, *61*, 981–986. https://doi.org/10.1515/amm-2016-0167.
36. Kabsch, W. A solution for the best rotation to relate two sets of vectors. *Acta Crystallogr. A* **1976**, *32*, 922–923. https://doi.org/10.1107/S0567739476001873.
37. Kabsch, W. A discussion of the solution for the best rotation to relate two sets of vectors. *Acta Crystallogr. A* **1978**, *34*, 827–828. https://doi.org/10.1107/S0567739478001680.
38. Umeyama, S. Least-squares estimation of transformation parameters between two point patterns. *IEEE Trans. Pattern Anal. Mach. Intell.* **1991**, *13*, 376–380. https://doi.org/10.1109/34.88573.
39. *ISO 6507-1:2018*. Metallic Materials—Vickers Hardness Test—Part 1: Test Method; International Organization for Standardization: Geneva, Switzerland, 2018.
40. Guo, Y.; Wang, Z.; Liu, Y.; Xiong, J.; Zhang, J.; Zhang, H. Study on Residual Stress Distribution in Stellite−6 Cladding Layers on 420 Steel Steam Turbine Blades. *J. Mater. Eng. Perform.* **2023**, *33*, 9214–9225. https://doi.org/10.1007/s11665-023-08560-7.
41. Ya, W.; Pathiraj, B. Residual stresses in Stellite 6 layers cladded on AISI 420 steel plates with a Nd:YAG laser. *J. Laser Appl.* **2018**, *30*, 032007. https://doi.org/10.2351/1.5039858.
42. Betsofen, S.Y.; Grigorovich, K.V.; Ashmarin, A.A.; Abdurashitov, A.Y.; Lebedev, M.A. Peculiarities of Formation of Residual Stresses in Welded Joints and Stellite Weld Cladding on Rail Steel. *Inorg. Mater. Appl. Res.* **2020**, *11*, 634–640. https://doi.org/10.1134/s2075113320030053.

Disclaimer/Publisher's Note: The statements, opinions and data contained in all publications are solely those of the individual author(s) and contributor(s) and not of MDPI and/or the editor(s). MDPI and/or the editor(s) disclaim responsibility for any injury to people or property resulting from any ideas, methods, instructions or products referred to in the content.